JMEPEG (2019) 28:5127–5137
https://doi.org/10.1007/s11665-019-04204-x

1059-9495/$19.00

Study of Thermomechanical Behavior of Zirconium-0.3 Tin Alloy

S.K. Jha, Saurabh Dixit, and Dinesh Srivastava

(Submitted January 21, 2019; in revised form June 2, 2019; published online July 12, 2019)

Zirconium-based alloys are used in the manufacturing of nuclear fuel tubes. These tubes need to be clad with zirconium-tin (Zr-0.3 wt.% Sn) alloy to enhance the lives of tubes. Manufacturing of such clad tubes is a challenging task, due to work hardening and dynamic softening phenomenon. In this study, hot deformation behavior of Zr-0.3Sn alloy is investigated at different temperatures and strain rates. It is found that fully recrystallized microstructure can be obtained by working at around 900 °C and high strain rate of 10 s^{-1}. Further, constitutive equations are developed for the entire domain of deformation range and fitted into standard FEM-based simulation model for extrusion. The simulation results are validated with experimental data. The difference in flow stresses values obtained from numerical and experimental methods was around 14%.

Keywords hot deformation, processing maps, Zr-Sn alloy

1. Introduction

Zirconium barrier cladding tubes are used for high burn-up nuclear fuels for BWRs (boiling water reactors) and PHWRs (pressurized heavy water reactor) (Ref 1-3). These cladding tubes are manufactured by co-extruding composite tube shell of zircaloy-2 and -4 with a liner of dilute zirconium-tin alloy (Zr-0.3Sn) at temperatures above 600 °C. Stress corrosion cracking (SCC) of zircaloy tubes is common under the radiating atmosphere of the nuclear reactor, without any protective inner layer. Hence, these tubes are cladded with Zr-0.3Sn alloy to prevent the SCC. This thin ductile layer arrests the crack within the layer. A good metallurgical bond is required between the tube and the clad to achieve high durability life of these fuel tubes. Manufacturing of such uniform layer of Zr-0.3Sn alloy is a challenge because high-temperature deformation, i.e., extrusion, of these alloys is a complex process where both the work hardening and dynamic softening phenomena occur simultaneously. In addition to deformation parameters (like the strain rate and degree of deformation and temperature), variations in chemical composition and initial microstructure prior to deformation influence the phenomena significantly, which in turn affects the quality of the product. In the production of the co-extruded cladding tube shell, deformation parameters need to be optimized in terms of strain rate and temperature so that the interface between the two materials could be solely identified by the variation in chemical composition on moving from zirconium-tin base alloy to zircaloy (Ref 4, 5). Such characteristics indicate the formation of a good metallurgical bond which is a necessity for achieving good service performance of the composite tube. If the combination of extrinsic and intrinsic variables can be translated into metallurgical phenomena, such as dynamic recovery and dynamic recrystallization, it will be possible to optimize the process variables to obtain the required microstructure for Zr-0.3Sn alloy (Ref 6, 7).

Gegel et al. (Ref 8) proposed dynamic material model (DMM) which is a continuum mechanics-based mathematical model to express the plastic flow of metals at high temperatures. In the previous studies, attempts have been made to develop dynamic material model using hot deformation data (Ref 9-13). Prasad et al. (Ref 14) assumed that there is no storage of energy in the material during deformation. The input energy converts instantly irreversibly into two different forms, i.e., thermal and microstructural changes. This model serves as a bridge between the continuum mechanics and the microstructural changes occurring during hot deformation. The dissipated power is related to the rate of entropy production in metallurgical processes, and it is evaluated by partitioning the total power between rise in temperature and microstructural changes. In view of the visco-plastic nature of hot deformation, the strain rate sensitivity plays the role of power partitioning factor. This model particularly considers the workpiece as a dissipater of power and calculates the efficiency of power dissipation through microstructural changes in the workpiece as compared with an ideal linear dissipater. However, the model developed by Prasad (Ref 14) does not explain the concept of entropy relation with microstructure evaluation (Ref 15-17). The entropy can be related to the number of possible atomic arrangements (Ref 16). However, it is found experimentally that the DMM model predicts the flow behavior of metal precisely (Ref 9, 18-21). The concept of DMM is used in many studies to optimize the thermomechanical working of zirconium-based alloys (Ref 22-24).

A processing map can be generated using DMM which contains superimposed power dissipation map and instability map to delineate high-efficiency and instable regions (Ref 13, 25, 26). The processing map is qualitatively utilized to understand the constitutive flow behavior of the material (Ref

S. K. Jha, Homi Bhabha National Institute, Mumbai 400 094, India; Mishra Dhatu Nigam Ltd. (MIDHANI), Hyderabad 500058, India; and Nuclear Fuel Complex, Hyderabad, India; **Saurabh Dixit**, Mishra Dhatu Nigam Ltd. (MIDHANI), Hyderabad 500058, India; and **Dinesh Srivastava**, Homi Bhabha National Institute, Mumbai 400 094, India; and Nuclear Fuel Complex, Hyderabad, India. Contact e-mail: saurabhdixit11@gmail.com.

20, 22, 27-30). Such model can be used to generate the processing maps to understand the flow behavior of commercial purity of wrought zirconium-tin alloy. The processing map and hot deformation behavior of zircaloy-2 were studied by Chakravarrty et al. (Ref 27, 31). Hot deformation behavior of zircaloy-4 is also available in the literature (Ref 19, 32). However, there is limited knowledge available on the hot deformation behavior of as-cast Zr-0.3Sn alloy. The knowledge of hot deformation behavior of Zr-0.3Sn alloy would be useful in optimizing the process parameters for co-extrusion of Zr-based clad tubes (Ref 33). The co-extruded tube of zircaloy with a liner of Zr-0.3Sn alloy should have continuous interface with no oxide and grain boundaries at the interface for nuclear fuel tube application. The interface should be mainly identified by compositional change. Jha et al. showed the experimental and numerical simulation of co-extrusion of zircaloy with liner of Zr-0.3Sn alloy (Ref 33). However, thermomechanical properties of Zr-0.3Sn alloy remain still unexplored in that study.

The information available from the processing maps is helpful in the identification of safe and unsafe domains for deformation. However, this information is of limited significance in bulk deformation processes such as extrusion and forging where quite complex deformation conditions exist. The parameters in these processes need information such as the effect of ram velocity on strain rate variation, generation of temperature due to deformation along the cross section and effect of tool geometry on deformation pattern in the product. Constitutive modeling of alloy with processing maps can be used for realistic analysis of the deformation behavior of the material. Constitutive modeling is a technique which has been used for a number of materials, and these models show good agreement with experimental results (Ref 18, 34, 35).

On the other hand, numerical simulation has been widely applied in various metalforming processes to optimize the design of forming tools and process parameters (Ref 36-39). As the deformation mechanism of zirconium-based alloys is a complex process, the mechanism changes not only with the change in temperature and strain rate but also with strain. Therefore, it is required to have a constitutive equation of alloy which can be used for the entire domain of deformation range and fit into standard FEM-based simulation technique used for bulk deformation process. In order to simulate the material flow behavior under specified conditions, these constitutive equations serve as an interesting tool as these can be used to predict the flow stress and even the microstructure evolution during hot forming processes.

In this paper, deformation mechanism of as-cast zirconium-tin alloy with respect to microstructural stability is explained using power dissipation maps which are generated using the concept of the dynamic material model. Constitutive equations for as-cast Zr-0.3Sn alloy are developed using the experimental data. The information was used to validate the extrusion force at different temperatures and strain rates. Numerical simulation for the extrusion processes was developed where material flow properties were used from the constitutive equations. Further, the simulated extrusion load was compared with actual extrusion trails of Zr-0.3Sn billets to validate the accuracy of the constitutive equation developed in this study.

The results obtained from this study can be used to find the combination of extrinsic and intrinsic variables that can be translated into metallurgical phenomena, such as dynamic recovery and dynamic recrystallization. Eventually, it is possible to optimize the process variables to obtain the required microstructure for Zr-0.3Sn alloy using this information.

2. Experimental

The material used for this study was a cast Zr-0.3Sn dilute alloy (0.3 wt.% Sn). Samples were taken from double-melted ingot using vacuum arc remelting (VAR) for hot deformation studies. Cylindrical specimens of 15 mm height and 10 mm diameter were machined along the axial direction. The isothermal compression tests were carried out on a Gleeble-3500 thermomechanical simulator in the temperature range of 600-900 °C and strain rates of 1 , 5 and 10 s^{-1}. The flow stress data at 0.01 and 0.1 s^{-1} strain rates are taken from the previous study by Jha et al. (Ref 40). A graphite sheet was placed between the specimens and the crossheads of the anvil to reduce the friction during compression test. The temperatures of the specimens as well as the adiabatic temperature rise during compression at high strain rate (1 s^{-1}) were measured by two thermocouples attached directly to the middle area of the specimens. All specimens were deformed up to true strain of 0.69. During the hot compression run, the flow stress data were recorded automatically as a function of strain for each deformation temperature and strain rate by the software directly linked with Gleeble-3500. The change in the microstructure at different temperatures and strain rates was analyzed using electron back-scattered diffraction (EBSD) technique. EBSD mapping was carried out using the Oxford EBSD detector attached to the Carl Zeiss scanning electron microscopy (SEM). Extrusions of this alloy were carried out at 3780 Ton H.E.P. (horizontal extrusion press) for 50 mm X 8 mm WT tube. FEM simulation was carried out to simulate material flow during extrusion on a commercial finite element program HyperXtrude.

3. Results and Discussion

3.1 Stress–Strain Curves

True stress–strain curves of cast Zr-0.3Sn alloy obtained at different strain rates and temperatures are shown in Fig. 1, and these plots show a lot of variations in the flow behavior of material with respect to temperatures and strain rates. Two different types of flow curves can be seen in Fig. 1: Ones show continuous strain-hardening effect, i.e., flow stress increases with increasing strain, and others show no strain hardening, i.e., flow stress remains constant with increasing strain. The flow curves plotted for 600-700 °C show continuous strain hardening for all strain rates. And the flow curves at high temperature, especially above 800 °C, exhibit no strain hardening. This suggests that dynamic recovery and dynamic recrystallization (DRX) take place above 800 °C even at very low strains. Very low strain hardening can be seen between temperature ranges 700 °C and 800 °C.

3.2 Generation of Processing Maps

A process map is generated using flow stress data as a function of temperature and strain rates. Figure 1 shows

variation in flow stress values at various temperatures and strain rates obtained using hot compression test.

The flow stress (σ) variation is given by

$$\sigma = K\dot{\varepsilon}^{m} \quad \text{(Eq 1)}$$

where K = constant

With given strain rate ($\dot{\varepsilon}$) and temperature, curve is fitted using spline function. The relation between strain rate sensitivity (m) and strain rate ($\dot{\varepsilon}$) is given as:

From Eq 1,

$$m = \frac{\partial \ln \sigma}{\partial \ln \dot{\varepsilon}}$$

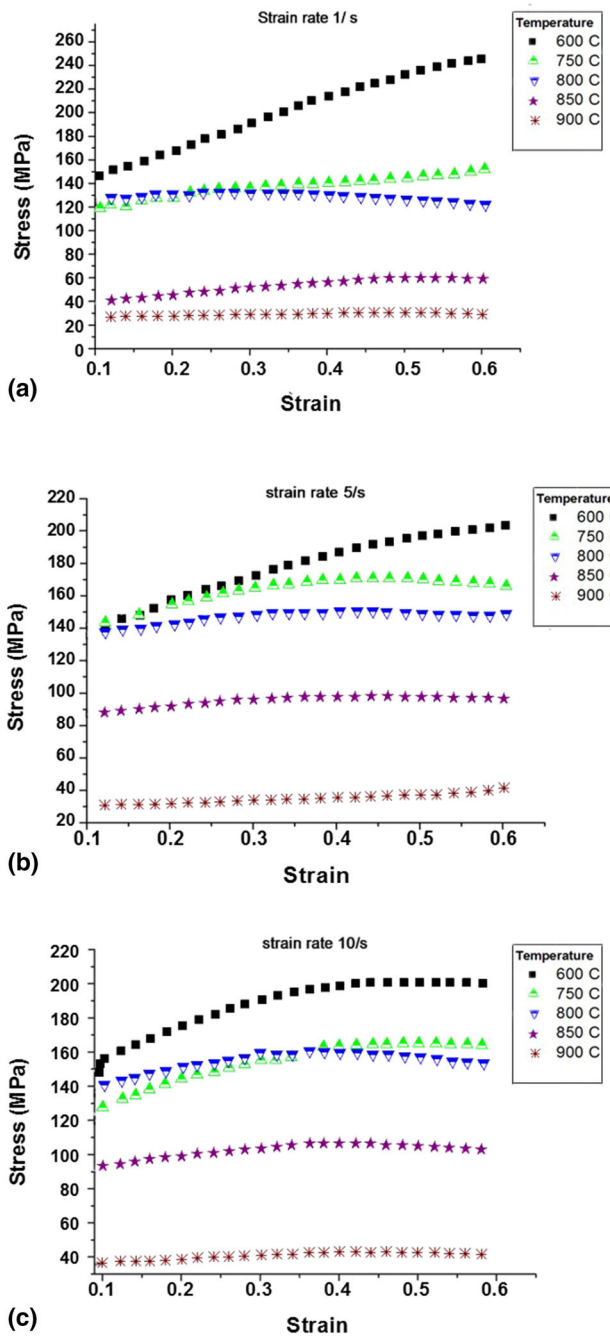

Fig. 1 Stress–strain curves of Zr-0.3Sn at various temperatures and strain rates: (a) 1 s^{-1}, (b) 5 s^{-1}, (c) 10 s^{-1}

The efficiency of power dissipation is given by:

$$\eta = \frac{2m}{(m+1)} \quad \text{(Eq 2)}$$

The flow instability parameter related is given by (Ref 14)

$$\xi = \frac{\partial \ln(m/m+1)}{\partial \ln \dot{\varepsilon}} + m < 0 \quad \text{(Eq 3)}$$

The efficiency of power dissipation is calculated and plotted as a contour map in a frame of temperatures and strain rates (Fig. 2). The variation in efficiency of power dissipation with temperatures and strain rates is referred as power dissipation map. This map is spanned by various domains in which specific microstructure mechanism occurs.

$\xi(\dot{\varepsilon})$ is calculated and plotted as a function of temperatures and strain rates. The regime where it is negative denotes flow instabilities. These plots are called as instability maps. The physical meaning of the above instability criterion is that if the system is not able to generate entropy at a rate that closely corresponds with the imposed rate, the system will localize the flow and cause flow instability.

A processing map is superimposition of power dissipation map and instability map to delineate regions of high efficiency and instability. Figure 2 shows processing map for Zr-0.3Sn dilute alloy. Contours with solid lines represent the efficiency of power dissipation, whereas shaded region indicates the instability domain. Map developed for Zr-0.3Sn alloy exhibits several domains safe for processing in terms of combination of temperature and strain rate and also contains regimes of flow instabilities and cracking. In general, the safe domains represent atomistic mechanisms such as dynamic recrystallization, dynamic recovery and superplasticity. The damage processes generally include ductile fracture at hard particles, wedge cracking, inter-crystalline cracking and cracking along prior particle boundaries, while the instability processes include flow localization, adiabatic shear band formation, flow rotations and dynamic strain aging. The safe domain of metal working facilitates a controlled microstructure of the hot-worked material.

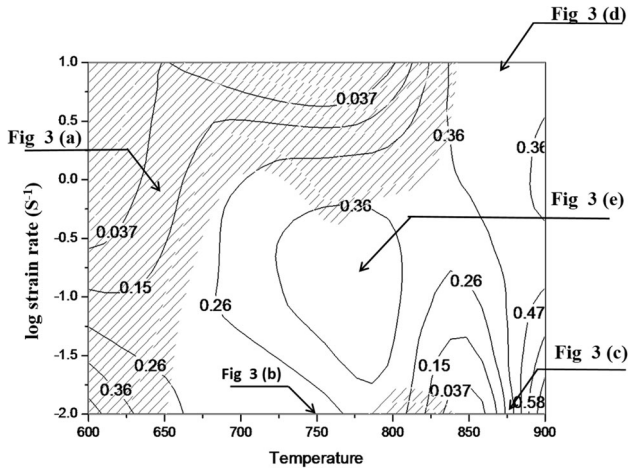

Fig. 2 Processing map of Zr-0.3Sn alloy at 0.6 strain. The instability region ($\xi < 0$) is presented in the form of shaded region. Microstructures from the locations marked on the processing map are presented in Fig. 3(a), (b), (c) and (d)

3.3 Validation of Processing Map

At lower temperatures, i.e., between 600 to 650 °C, no stable regions for deformation are observed for any combination of temperature and strain rate. The microstructure of alloy deformed at 650 °C with the strain rate of 1 s^{-1} in Fig. 3(a) shows the localized flow of large cast grains surrounded by heavily deformed grains. Nonuniform deformation takes place due to the favorable orientation of few cast grains in the direction of applied stress. Such kind of microstructure is undesirable in metalworking operations. Hence, these processing conditions should be avoided. Between 700 to 800 °C at low strain rates, alloy deforms with high deformation efficiency; however, as strain rate increases beyond 1 s^{-1}, again deformation domain falls in instability region. This inconsistency in deformation behavior is mainly due to the presence of large columnar grains in cast Zr-0.3Sn alloy. With an increase in temperature beyond 700 °C, there is sufficient energy available to initiate the nucleation and growth of new grains. However, to deform the material with dynamic recrystallization, there is a need for lower strain rate which will support nucleation and growth of new grains. Figure 3(b) shows fully recrystallized grains of Zr-0.3Sn alloy deformed at 750 °C at 0.01 s^{-1} strain rate. The maximum efficiency of power dissipation is about 40-50% for as-cast Zr-0.3Sn alloy obtained in the high temperature range between 875 to 900 °C Fig. 3(c) and (d). Results indicate that fully recrystallized structure can

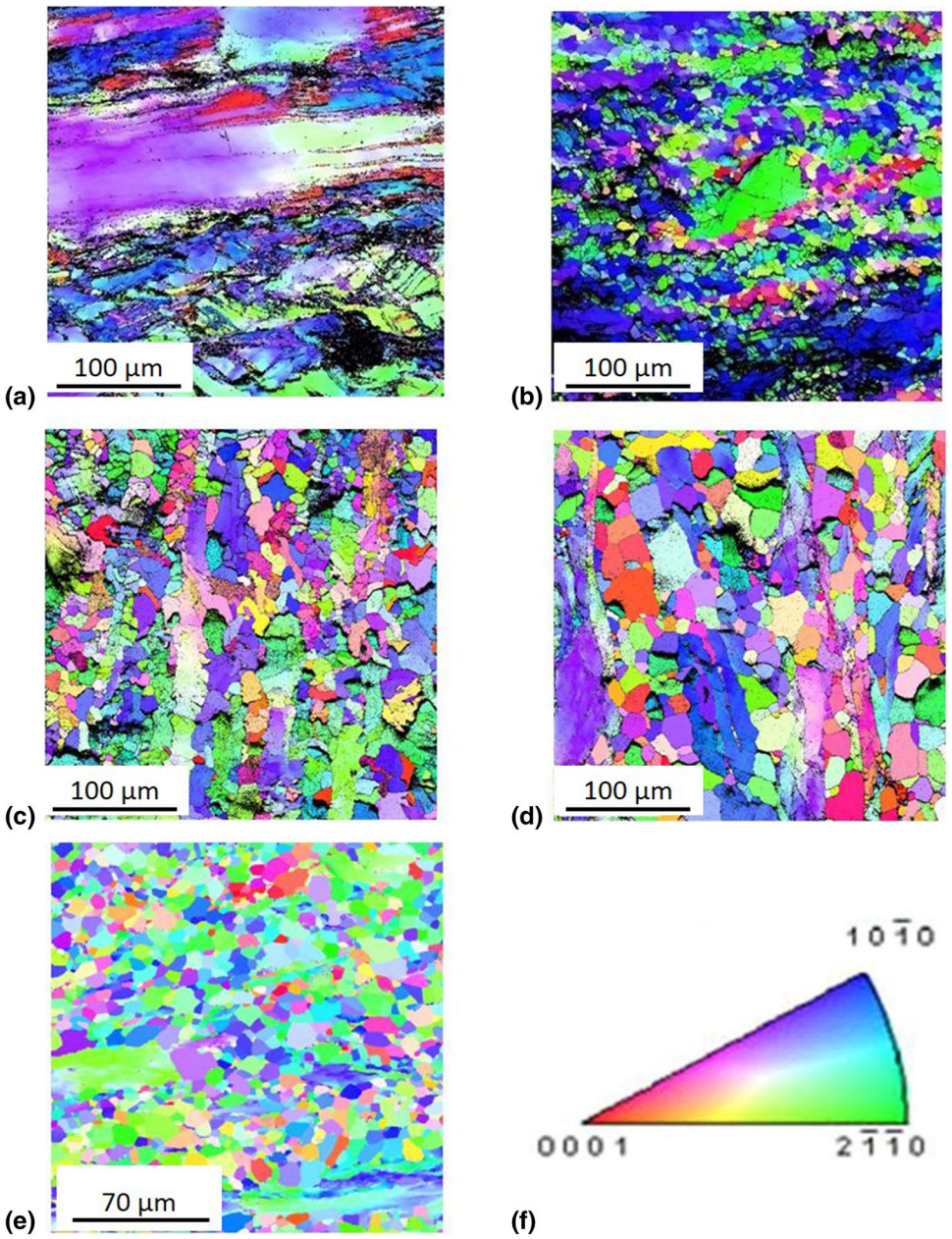

Fig. 3 EBSD micrograph of deformed Zr-0.3Sn alloy (a) at 650 °C at strain rate and 1 s^{-1}. (b) Fully deformed and recrystallized microstructure of Zr-0.3Sn alloy deformed at 750 °C and $10^{-2}s^{-1}$. (c) Fully deformed and recrystallized microstructure at 875 °C and $10^{-2}s^{-1}$. (d) Fully deformed and recrystallized microstructure at 875 °C and 10 s^{-1}. (e) Fully recrystallized uniform microstructure at 775 °C and 0.1 s^{-1}. (f) IPF map for the images

be achieved by bulk deformation of this alloy at high strain rate and high temperature.

3.4 Development of Constitutive Modeling

To analyze the deformation behavior of an alloy without conducting actual deformation trials, the FEM-based simulation is useful but it requires an empirical relationship between stress and strain at different temperatures and strain rates expressions in terms of material constants. Based on the previous studies (Ref 41, 42), it is clear that the mechanism of deformation changes with the change in deformation parameters and has significant effect on material constants. Development of single constitutive equation that is valid for the entire range of deformation regime (in terms of strain rates, strains and temperatures) is desirable for facilitating the FEM-based simulation of the actual industrial deformation process in order to achieve the optimized processing conditions.

3.4.1 Basis of Constitutive Modeling. High-temperature deformation of an alloy occurs by simultaneous application of stress and temperature where strain rate plays an important role as compared to strain; hence, it is the strain rate that is empirically related to temperature. The effect of temperature and strain rate on the deformation behavior of the material is usually expressed using a temperature-compensated strain rate parameter or Zener–Holloman parameter (Z) in terms of an exponential equation (Ref 43). The flow stress, strain rate and temperature can be expressed by Arrhenius-type equation (Ref 10, 18, 35). These equations are given as:

$$Z = \dot{\varepsilon}\exp\left(\frac{Q}{RT}\right) = A(\sinh(\alpha\sigma)^n \quad \text{(Eq 4)}$$

$$\dot{\varepsilon} = Af(\sigma)\exp\left(\frac{-Q}{RT}\right) \quad \text{(Eq 5)}$$

where $f(\sigma)$ depends on the level of stress and it is defined as:

$$f(\sigma) = \begin{cases} \sigma^n & \text{for } \alpha\sigma < 0.8 \\ \exp(\beta\sigma) & \text{for } \alpha\sigma > 1.2 \\ |\sinh(\alpha\sigma)|^n & \text{for all } \alpha\sigma \end{cases} \quad \text{(Eq 6)}$$

In the above equation, $\dot{\varepsilon}$ is strain rate, A, n, β, α and Q are material constants, α is identified as stress level parameter ($mm^2 N^{-1}$), n is stress exponent, A is called structure factor (s^{-1}), β, n and α are related as $\beta = \alpha n$ and Q is thermal activation energy (kJ/mol). Thermal activation energy is an important material constant. It is related to mechanical properties in the process of thermal deformation and reflects the degree of difficulty of thermal deformation. In the above equation, R is the gas constant (J/(molK)) and T is the absolute temperature (K).

3.4.2 Determination of Material Constants. Strain rate $\dot{\varepsilon}$ is related to various material constants as follows:

$$\dot{\varepsilon} = B\sigma^n \quad \text{(Eq 7)}$$

$$\dot{\varepsilon} = C\exp(\beta\alpha) \quad \text{(Eq 8)}$$

Flow stress data obtained from the isothermal hot compression tests at different strain rates were used to estimate the material constants. The material constants A, n, α, β and Q are estimated by using the variation in flow stress with temperature and strain rate for a true plastic strain of 0.6. Similar procedure has been used for estimating the material constants at other strains as well.

Next, by taking logarithm on both sides of Eq 7 and 8, it is possible to estimate the following relationship between flow stress and strain rate with material constants n and β given as:

$$\ln(\sigma) = \frac{1}{n}\ln(\dot{\varepsilon}) - \frac{1}{n}\ln(\beta) \quad \text{(Eq 9)}$$

$$\sigma = \frac{1}{\beta}\ln(\dot{\varepsilon}) - \frac{1}{\beta}\ln(C) \quad \text{(Eq 10)}$$

Equation 9 and 10 represents a straight line, and hence the values of n and β can be obtained from the slope of lnσ v/s ln $\dot{\varepsilon}$ and σ v/s ln $\dot{\varepsilon}$ plots as shown in Fig. 4(a) and (b), respectively. The lines are apparently parallel to each other, and hence the mean values of slopes are taken as n and β. α, stress level parameter, is calculated from the average value of n and β using $\alpha = \beta/n$ relationship.

3.4.3 Determination of Activation Energy (Q) and Value of Stress Exponent (n). Activation energy (Q) plays an important role in constitutive equation. Activation energy in hot deformation indicates the degree of difficulty during plastic

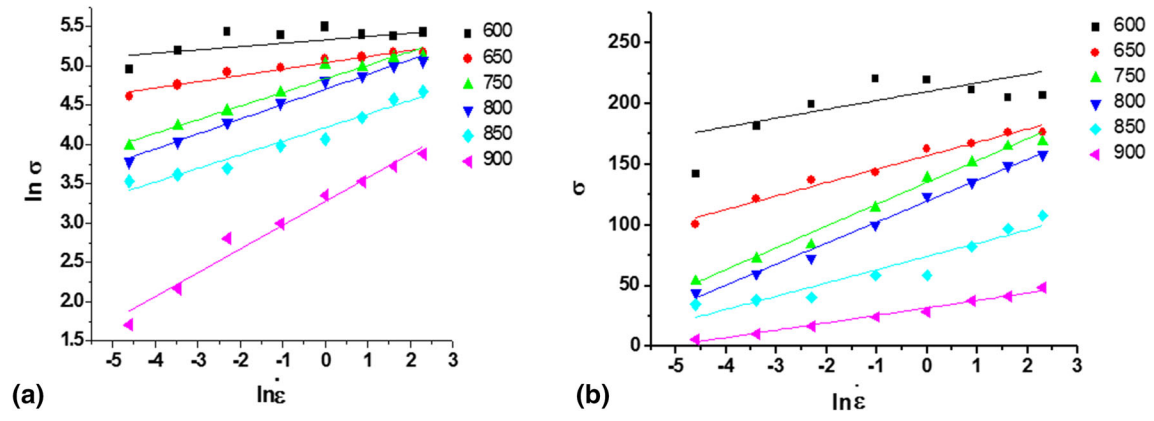

Fig. 4 (a) Plot of ln σ v/s ln $\dot{\varepsilon}$ slope of the lines gives the value of n (b). Plot of σ v/s ln $\dot{\varepsilon}$ slope of the lines gives the value of β

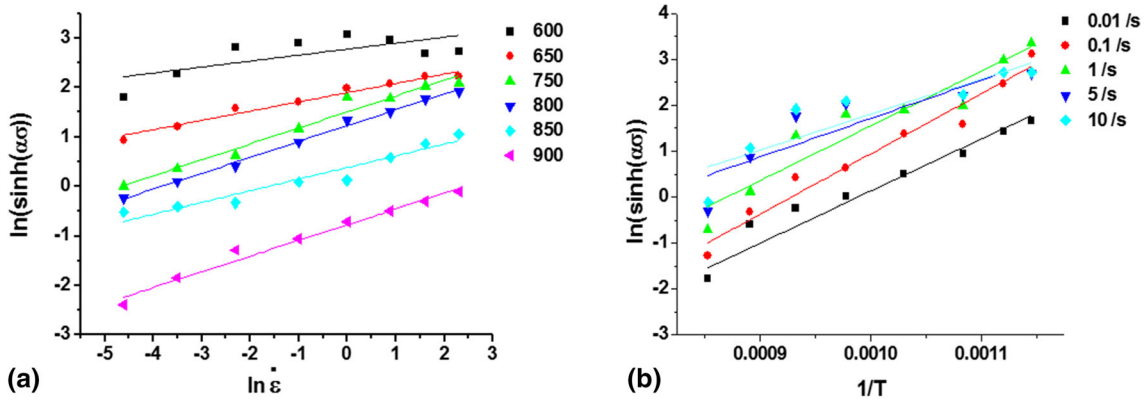

Fig. 5 Plot of (a) ln[sinh(ασ)] vs. $\ln \dot{\varepsilon}$ and (b) ln[sinh(ασ)] vs. 1/T

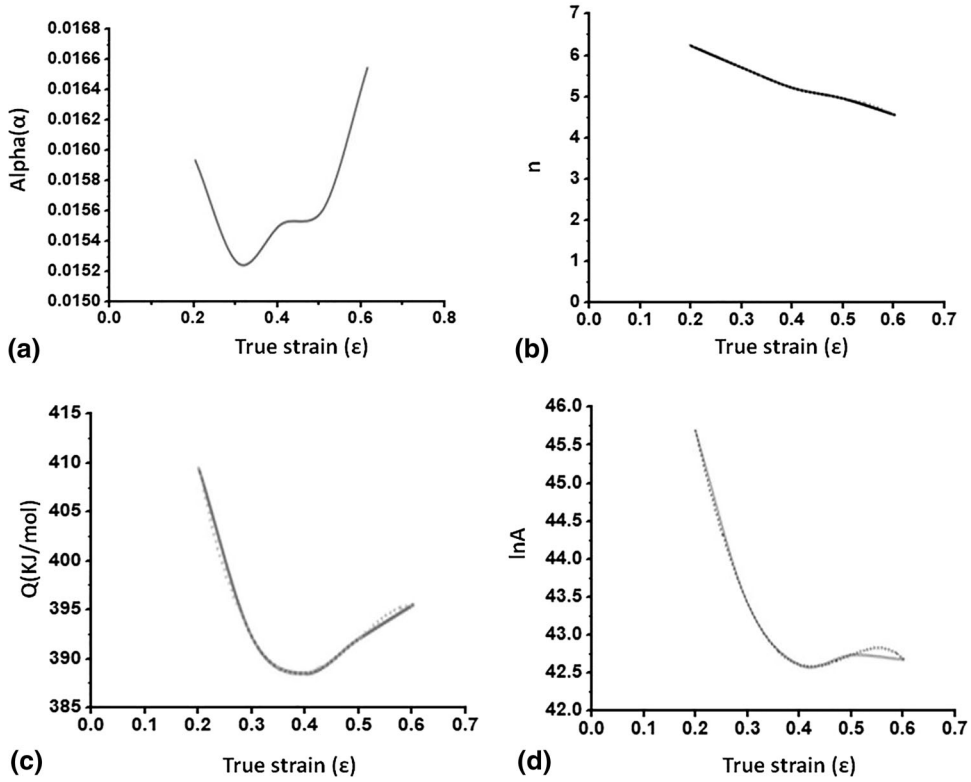

Fig. 6 Plot of (a) alpha (α) vs. true strain (ε) shows minimum value at 0.3 strain and maximum value at 0.60 strain, (b) *n* vs. true strain (ε) shows continuous decrease in its value with strain, (c) activation energy (*Q*) vs. true strain (ε) shows a minima at 0.4 strain and (d) ln *A* vs. true strain (ε) shows decreasing trend with strain

deformation. The values of activation energy are characteristic of composition and microstructure of the material (Ref 44, 45). It also gives an idea about softening mechanism activated during the deformation. DRX will contribute to the softening when the *Q* value is much lower than the diffusion activation energy, and dynamic recovery will contribute to softening when *Q* value approaches the diffusion activation energy (Ref 46).

For zirconium and dilute Zr-0.3Sn alloy, value of activation energy has been determined for wrought material; however, for as-cast material, data are not available. To determine the value of *Q*, sine hyperbolic equation which takes care of low and high stress values was used.

For flow stress, Eq 5 can be written as:

$$\dot{\varepsilon} = A[\sinh(\alpha\sigma)]^n \exp\left(\frac{Q}{RT}\right) \quad \text{(Eq 11)}$$

Taking logarithm on both sides of Eq 11 gives:

$$\ln[\sinh(\alpha\sigma)] = \frac{\ln \dot{\varepsilon}}{n} + \frac{Q}{nRT} - \frac{\ln A}{n} \quad \text{(Eq 12)}$$

The data of flow stress at different strain rates and different temperatures have been used to draw a plot as per Eq 12 (Fig. 5a). The flow stress data corresponding to strain rates 1, 5 and 10 s^{-1} are taken from Fig. 1, while 0.01 and 0.1 s^{-1} strain rates are taken from the previous study by Jha et al. (Ref 40).

The slope of ln $\dot{\varepsilon}$ versus ln[sinh(ασ)] gives value of 1/n and reciprocal of this n at different temperatures. The mean value of n is obtained by taking average of the values of n at different temperature. The mean value of n by this method was 4.53.

Next, in Eq 12, keeping the value of strain rate fixed, linear plots are drawn with 1/T at X-axis and ln[sinh(ασ)] at Y-axis. A number of straight lines are obtained for different strain rates, and using average value of slopes for different strain rates, the value of Q/nR is calculated, in which R is gas constant and n is calculated from the previous graph. After taking the average for all strain rates, the value of Q obtained is 395.56 kJ/mol. The value of A was calculated using Fig. 5(b) for different strain rates. The average calculated value of A is 3.36 E + 18.

The constitutive equation for flow stress (σ_p) related to the deformation temperature and strain rate of Zr-0.3Sn alloy can be expressed using sine hyperbolic function; by considering Eq 4, 5 and 11, constitutive equation can be expressed as (Ref 47, 48):

$$\sigma_p = \frac{1}{\alpha}\sinh^{-1}\left(\frac{\dot{\varepsilon}\exp(Q/RT)}{A}\right)^{1/n} \quad \text{(Eq 13)}$$

Equation 13 facilitates the estimation of flow stress at a given strain rate and temperature for known values of material constants.

3.4.4 Strain-Compensated Arrhenius Model. From Eq 13, it is obvious that the influence of strain is not taken into account in Arrhenius model. However, it has been reported that the deformation activation energy and other material constants are significantly affected by strain (Ref 18, 34, 35, 49). Flow stress usually varies with strain, especially on occurrence of dynamic recrystallization, which could cause the obvious decrease in flow stress. Thus, Arrhenius model might not be appropriate for describing the dynamic softening phenomenon. Further, in order to provide more precise prediction of flow stress, the strain-compensated Arrhenius model is developed considering the effect of strain on all material constants.

To find the effect of strain on material constants α, Q, n and A under different strains, similar steps as used earlier in case of strain rate of 0.6 are adopted from strain values of 0.1 to 0.6 in the interval of 0.1. The resulting values obtained for all constants were plotted against strain (Fig. 6). Polynomial fit of fourth order was found to be suitable to find constants for empirical equations; higher order polynomial would over-fit and become too sensitive, thus losing the ability of true representation.

$$\alpha = B_0 + B_1\varepsilon + B_2\varepsilon^2 + B_3\varepsilon^3 + B_4\varepsilon^4 \quad \text{(Eq 15)}$$

$$n = C_0 + C_1\varepsilon + C_2\varepsilon^2 + C_3\varepsilon^3 + C_4\varepsilon^4 \quad \text{(Eq 16)}$$

$$Q = D_0 + D_1\varepsilon + D_2\varepsilon^2 + D_3\varepsilon^3 + D_4\varepsilon^4 \quad \text{(Eq 17)}$$

$$\ln A = E_0 + E_1\varepsilon + E_2\varepsilon^2 + E_3\varepsilon^3 + E_4\varepsilon^4 \quad \text{(Eq 18)}$$

3.4.5 Effect of Strain on Material Constants. In order to delineate the effect of strain on material constants, these constants are plotted against strain as shown in Fig. 6. Figure 6(a) shows the dependence of stress level parameters (α) on strain. Its value remains nearly constant in medium-strain region but increases at both lower and higher strains. Another material constant, i.e., stress exponent (n), is seen to decrease gradually with the increasing value of strain (Fig. 6(b)). This effect is mainly due to the reduced effect of strain hardening during deformation at high temperature and high strain. Activation energy (Q) has a significant effect on strain as can be seen from Fig. 6(c). Initially, it decreases drastically with increasing strain reaching its minimum value at around 0.4 strain, beyond which it increases with increasing strain. A is a structure constant, and its value decreases continuously with increasing strain value (Fig. 6(d)).

Equations for material constants are derived by polynomial curve fitting of plots shown in Fig. 6. These equations are given below as:

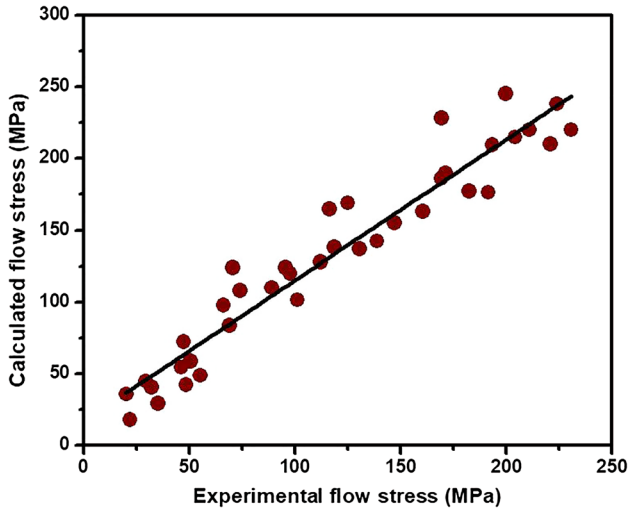

Fig. 7 Comparison between calculated flow stress and experimental flow stress reveals a linear fit

Table 1 Coefficients of polynomial fitting curves for material constants

α		N		Q		lnA	
B_0	.0347	C_0	3.6422	D_0	506.22	E_0	53.365
B_1	− 0.2091	C_1	40.123	D_1	− 730.03	E_1	− 39.774
B_2	0.817	C_2	− 201.32	D_2	1345.3	E_2	− 40.405
B_3	− 1.3775	C_3	373.51	D_3	− 466.67	E_3	287.21
B_4	0.85420	C_4	− 242.19	D_4	− 433.33	E_4	− 264.92

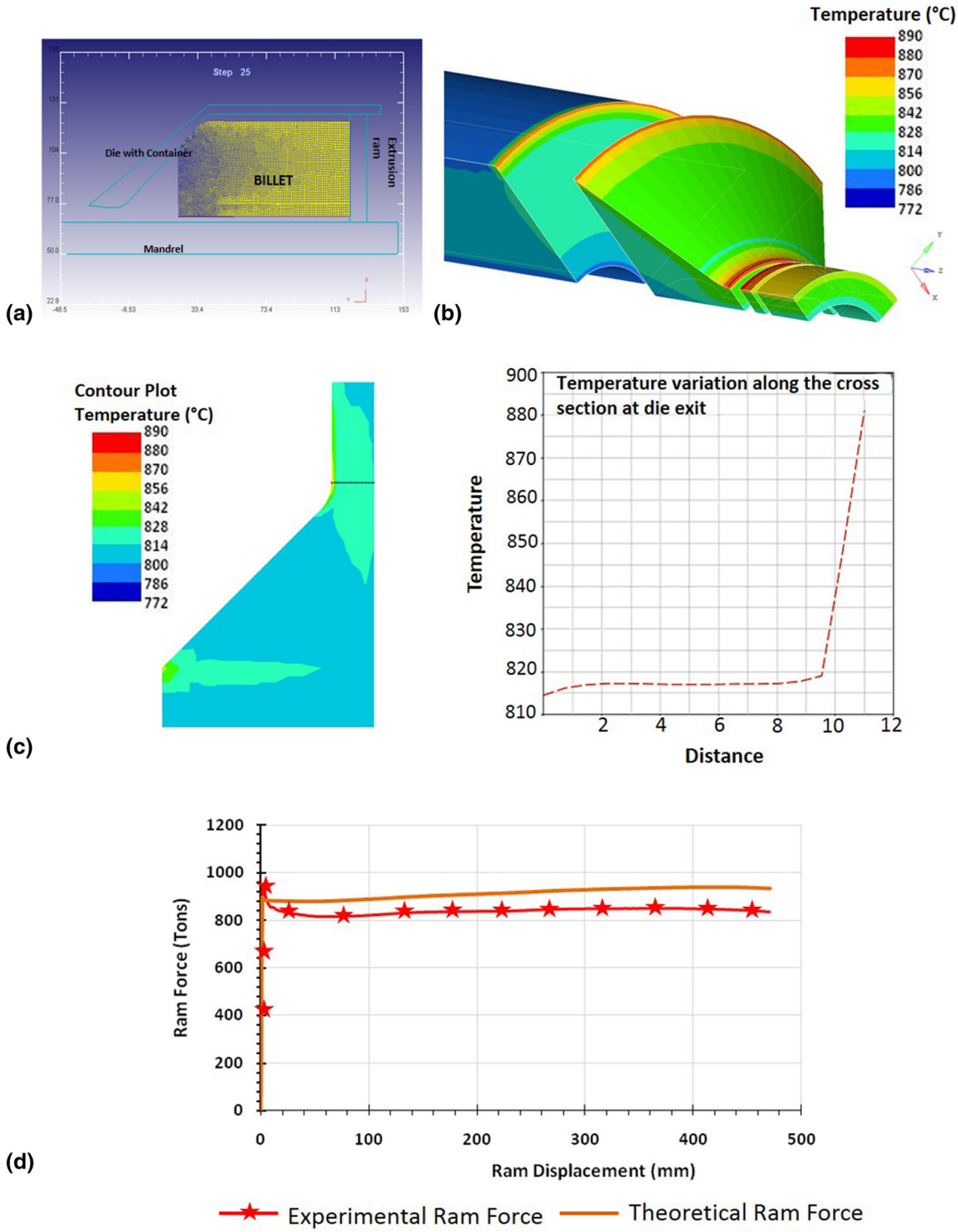

Fig. 8 Simulation of extrusion process. (a) GUI model of extrusion process. (b) Color contour shows temperature variation during the extrusion. (c) Temperature profile along the thickness of the tube during the extrusion. (d) Experimental and theoretically calculated ram forces v/s ram displacements; theoretically calculated forces shows good correlation with experimentally obtained forces

$$\alpha = 0.8542\varepsilon^4 - 1.3775\varepsilon^3 + 0.817\varepsilon^2 - 0.2091\varepsilon + 0.0347$$
$$n = -242.19\varepsilon^4 + 373.51\varepsilon^3 - 201.32\varepsilon^2 + 40.123\varepsilon + 3.6422$$
$$Q = -433.33\varepsilon^4 - 466.67\varepsilon^3 + 1345.3\varepsilon^2 - 730.03\varepsilon + 506.22$$
$$\ln A = -264.92\varepsilon^4 + 287.21\varepsilon^3 - 40.405\varepsilon^2 - 39.774\varepsilon + 53.365$$

The values of fitted constants obtained from above equations are listed in Table 1. Flow stress of Zr-0.3Sn alloy for different values of strain, strain rates and temperatures can be obtained by substituting these values of material constants in the constitutive equation (Eq 13). To check the accuracy of the constitutive equation, value of flow stress obtained using Eq 13

and value obtained from experimental data for various processing conditions were compared against each other as shown in Fig. 7. The correlation coefficient is 0.92. This suggests close correspondence between theoretical and experimental results of flow stresses.

3.5 Validation of Constitutive Equation

The finite element method has been the most commonly used technique to simulate metalforming processes. HyperXtrude software makes use of finite element model based on Zener–Holloman relation as given in Eq 4, 5 and 6 and using various constant values obtained for Zr-0.3Sn alloy. Lagrangian–Eulerian formulation was used to compute velocity, temperature, stress, strain and pressure in the flow field. The stress data are used to calculate forces acting on tool. This technique has been used with a variety of approaches including Lagrangian, Eulerian and more recently arbitrary Lagrangian–Eulerian (ALE) (Ref 50, 51). The issue of mesh distortion and difficulties faced in tracing free surface during the extrusion simulation can be addressed using ALE method.

The principles of conservation of mass, momentum and energy are used for writing the governing equations to determine flow and heat transfer in incompressible viscous fluids. These equations are written in terms of primitive variables (velocity, pressure and temperature) with reference to a Eulerian frame, i.e., a space-fixed system of coordinates through which the fluid flows.

Meshing was done using nonuniform quadrilateral elements. The simulations are performed within the framework of following simplifying assumptions: (a) constant heat transfer and friction coefficients between workpiece and tools throughout the extrusion process; (b) only plastic deformation of workpiece occurs; (c) about 90% of deformation work is dissipated as heat; (d) perfect rigidity of the extrusion tools; (e) and uniformity of initial workpiece temperature. The simulation was successfully carried out by giving a sticking condition on entire length of the liner. The GUI (graphical user interface) images of simulation showing die mandrel and billet are shown in Fig. 8(a). Temperature of billet was set to 820 °C at the start of simulation.

Figure 8(b) and (c) shows the simulation result of extrusion of Zr-0.3Sn alloy, and the color couture denotes the temperature variation during the extrusion. The process (extrusion) load values were validated for actual extrusion of Zr-0.3Sn alloy. The actual force required for extrusion process and force obtained by simulation using constitutive equations (Eq 13) are plotted in Fig. 8(d). It can be seen from Fig. 8(d) that FEM simulation precisely estimates the force required for the extrusion. The deviation between actual force required and force obtained by simulation is around 8%. The deviation is possibly due to variation in the activation energy of the material at different temperatures and strain rates.

4. Conclusions

Co-extrusion of Zr-0.3Sn-lined zircaloy-2 tubes at elevated temperature requires optimization of extrusion parameters. Deformation behavior of liner material (Zr-0.3Sn alloy) was studied using hot compression testing method at different temperatures and strain rates. Processing map for Zr-0.3Sn alloy has been developed using thermomechanical data. The map so developed systematically explains the influence of temperature and strain rate on the constitutive flow behavior of cast Zr-0.3Sn alloy. Different regions of processing maps have been validated by microstructural evidences. It is also observed that while working in the beta phase region of the alloy at $\sim$ 900 °C and high strain rate of 10 s^{-1}, a fully recrystallized structure can be obtained. This result has significant influence on the industrial applications since at high temperatures flow stress is extremely low, and therefore, with less force and high rate of deformation, it is possible to get the fully recrystallized product. This type of processing map is useful for bulk deformation process and can be utilized in industrial practice.

The constitutive equation has been developed for cast Zr-0.3Sn alloy for FEM-based simulation and modeling of hot deformation process. Since deformation of as-cast material is inhomogeneous, which was observed from true strain versus flow stress curves, it was difficult to obtain a constitutive equation that is valid over the entire range of deformation conditions. Hence, strain-compensated constitutive equation has been developed for cast Zr-0.3Sn alloy. Flow stress data obtained from this equation exhibit around 14% deviation from experimental data, and this deviation is mainly in lower temperatures and higher strain rates regimes.

The variation in results is observed due to variation in the activation energy of the material at different temperatures and strain rates. The constitutive equation was also validated using simulation of extrusion process where extrusion forces were calculated using this equation and were compared with the actual forces generated during the experimental extrusion process. The difference in values of forces obtained from these methods is around 8%.

References

1. D.O. Northwood, The Development and Applications of Zirconium Alloys, *Mater. Des.*, 1985, **6**, p 58–70. https://doi.org/10.1016/0261-3069(85)90165-7
2. L. Hallstadius, S. Johnson, and E. Lahoda, Cladding for high Performance Fuel, *Prog. Nucl. Energy*, 2012, **57**, p 71–76. https://doi.org/10.1016/j.pnucene.2011.10.008
3. R. Krishnan and M. Asundi, Zirconium Alloys in Nuclear Technology, *Proc Indian Acad SciEngg Sci.*, 1981, **4**, p 41–56
4. L.F.P. Van Swam and C.M. Eucken, ASTM Committee B-10 on Reactive and Refractory Metals and Alloys, International Atomic Energy Agency, eds., Zirconium in the nuclear industry: eighth international symposium, ASTM, Philadelphia, PA, 1989
5. K. Edsinger and K.L. Murty, LWR Pellet-Cladding Interactions: Materials Solutions to SCC, *JOM*, 2001, **53**, p 9–13. https://doi.org/10.1007/s11837-001-0079-7
6. B.A. Cheadle, C.E. Ells, and W. Evans, The Development of Texture in Zirconium Alloy Tubes, *J. Nucl. Mater.*, 1967, **23**, p 199–208. https://doi.org/10.1016/0022-3115(67)90065-7
7. Z. Chen, K. Ikeda, T. Murakami, T. Takeda, and J.-X. Xie, Fabrication of Composite Pipes by Multi-Billet Extrusion Technique, *J. Mater. Process. Technol.*, 2003, **137**, p 10–16. https://doi.org/10.1016/S0924-0136(02)01052-X
8. H. Gegel, in Experimental Verification of Process Models (1983)
9. Y.V.R.K. Prasad, Author's Reply: Dynamic Materials Model: Basis and Principles, *Metall. Mater. Trans. A*, 1996, **27**, p 235–236. https://doi.org/10.1007/BF02647765
10. Y.V.R.K. Prasad, H.L. Gegel, S.M. Doraivelu, J.C. Malas, J.T. Morgan, K.A. Lark, and D.R. Barker, Modeling of Dynamic Material Behavior in Hot Deformation: Forging of Ti-6242, *Metall. Trans. A*, 1984, **15**, p 1883–1892. https://doi.org/10.1007/BF02664902

11. H. Sun, Y. Zhang, A.A. Volinsky, B. Wang, B. Tian, K. Song, Z. Chai, and Y. Liu, Effects of Ag Addition on Hot Deformation Behavior of Cu-Ni-Si Alloys: Effects of Ag Addition on Hot Deformation Behavior…, *Adv. Eng. Mater.*, 2017, **19**, p 1600607. https://doi.org/10.1002/adem.201600607
12. Y. Zhang, H. Sun, A.A. Volinsky, B. Wang, B. Tian, Z. Chai, Y. Liu, and K. Song, Small Y Addition Effects on Hot Deformation Behavior of Copper-Matrix Alloys, *Adv. Eng. Mater.*, 2017, **19**, p 1700197. https://doi.org/10.1002/adem.201700197
13. Y. Zhang, H. Sun, A.A. Volinsky, B. Wang, B. Tian, Y. Liu, and K. Song, Constitutive Model for Hot Deformation of the Cu-Zr-Ce Alloy, *J. Mater. Eng. Perform.*, 2018, **27**, p 728–738. https://doi.org/10.1007/s11665-018-3168-2
14. Y.V.R.K. Prasad and T. Seshacharyulu, Modelling of Hot Deformation for Microstructural Control, *Int. Mater. Rev.*, 1998, **43**, p 243–258. https://doi.org/10.1179/imr.1998.43.6.243
15. F. Montheillet, J.J. Jonas, and K.W. Neale, Modeling of Dynamic Material Behavior: A Critical Evaluation of the Dissipator Power Co-content Approach, *Metall. Mater. Trans. A*, 1996, **27**, p 232–235. https://doi.org/10.1007/BF02647764
16. S. Ghosh, Interpretation of Microstructural Evolution Using Dynamic Materials Modeling, *Metall. Mater. Trans. A.*, 2000, **31**, p 2973–2974. https://doi.org/10.1007/BF02830342
17. S. Ghosh, Interpretation of Flow Instability Using Dynamic Material Modeling, *Metall. Mater. Trans. A.*, 2002, **33**, p 1569–1572. https://doi.org/10.1007/s11661-002-0081-x
18. Y.C. Lin, Y.-C. Xia, X.-M. Chen, and M.-S. Chen, Constitutive Descriptions for Hot Compressed 2124-T851 Aluminum Alloy Over a Wide Range of Temperature and Strain Rate, *Comput. Mater. Sci.*, 2010, **50**, p 227–233. https://doi.org/10.1016/j.commatsci.2010.08.003
19. J.L. Derep, S. Ibrahim, R. Rouby, and G. Fantozzi, Deformation Behaviour of Zircaloy-4 Between 77 and 900 K, *Acta Metall.*, 1980, **28**, p 607–619. https://doi.org/10.1016/0001-6160(80)90127-3
20. D.-X. Wen, Y.C. Lin, H.-B. Li, X.-M. Chen, J. Deng, and L.-T. Li, Hot Deformation Behavior and Processing Map of a Typical Ni-Based Superalloy, *Mater. Sci. Eng. A.*, 2014, **591**, p 183–192. https://doi.org/10.1016/j.msea.2013.09.049
21. Y. Zhang, B. Tian, A.A. Volinsky, X. Chen, H. Sun, Z. Chai, P. Liu, and Y. Liu, Dynamic Recrystallization Model of the Cu-Cr-Zr-Ag Alloy Under Hot Deformation, *J. Mater. Res.*, 2016, **31**, p 1275–1285. https://doi.org/10.1557/jmr.2016.140
22. J.K. Chakravartty, G.K. Dey, S. Banerjee, and Y.V.R.K. Prasad, Characterization of Hot Deformation Behaviour of Zr□2.5Nb□0.5Cu Using Processing Maps, J. Nucl. Mater. 218 (1995) 247–255. https://doi.org/10.1016/0022-3115(94)00379-3
23. J.K. Chakravartty, Y.V.R.K. Prasad, and M.K. Asundi, Processing Map for Hot Working of Alpha-Zirconium, *Metall. Trans. A.*, 1991, **22**, p 829–836. https://doi.org/10.1007/BF02658992
24. Y.B. Tan, L.H. Yang, C. Tian, R.P. Liu, X.Y. Zhang, and W.C. Liu, Hot Deformation Behavior of ZrTiAlV Alloy with a Coarse Grain Structure in the β Phase Field, *Mater. Sci. Eng. A.*, 2013, **577**, p 218–224. https://doi.org/10.1016/j.msea.2013.04.056
25. S.K. Singh, K. Chattopadhyay, and P. Dutta, High-Temperature Workability of Thixocast A356 Aluminum Alloy, *Metall. Mater. Trans. A.*, 2015, **46**, p 3248–3259. https://doi.org/10.1007/s11661-015-2855-y
26. B.K. Raghunath, K. Raghukandan, R. Karthikeyan, K. Palanikumar, U.T.S. Pillai, and R.A. Gandhi, Flow Stress Modeling of AZ91 Magnesium Alloys at Elevated Temperature, *J. Alloys Compd.*, 2011, **509**, p 4992–4998. https://doi.org/10.1016/j.jallcom.2011.01.182
27. J.K. Chakravartty, S. Banerjee, Y.V.R.K. Prasad, and M.K. Asundi, Hot-Working Characteristics of Zircaloy-2 in the Temperature Range of 650-950 °C, *J. Nucl. Mater.*, 1992, **187**, p 260–271. https://doi.org/10.1016/0022-3115(92)90506-G
28. R. Kapoor and J.K. Chakravartty, Characterization of Hot Deformation Behaviour of Zr-2.5Nb in β phase, J. Nucl. Mater. 306 (2002) 126–133. https://doi.org/10.1016/s0022-3115(02)01290-4
29. J.K. Chakravartty, R. Kapoor, S. Banerjee, and Y.V.R.K. Prasad, Characterization of Hot Deformation Behavior of Zr-1Nb-1Sn Alloy, *J. Nucl. Mater.*, 2007, **362**, p 75–86. https://doi.org/10.1016/j.jnucmat.2006.11.007
30. S.K. Singh, K. Chattopadhyay, G. Phanikumar, and P. Dutta, Experimental and Numerical Studies on Friction Welding of Thixocast A356 Aluminum Alloy, *Acta Mater.*, 2014, **73**, p 177–185. https://doi.org/10.1016/j.actamat.2014.04.019
31. J. Chakravartty, Y. Prasad, and M. Asundi, Processing Map and Hot Working Characteristics of Zircaloy-2, in: C. Eucken, A. Garde (Eds.), Zircon. Nucl. Ind. Ninth Int. Symp., ASTM International, 100 Barr Harbor Drive, PO Box C700, West Conshohocken, PA 19428-2959, 1991: pp. 48-48–14. https://doi.org/10.1520/stp25498s
32. K.V.M. Krishna, S.K. Sahoo, I. Samajdar, S. Neogy, R. Tewari, D. Srivastava, G.K. Dey, G.H. Das, N. Saibaba, and S. Banarjee, Microstructural and Textural Developments During Zircaloy-4 Fuel Tube Fabrication, *J. Nucl. Mater.*, 2008, **383**, p 78–85. https://doi.org/10.1016/j.jnucmat.2008.08.050
33. S.K. Jha, S. Dixit, K. Chetan, K. Vaibhaw, and D. Srivastava, Co-extrusion of Zircaloy-2 and Zr-Sn Alloy for Double Clad Tube Manufacturing: Numerical Simulation and Experimental Validation, *J. Manuf. Process.*, 2019, **39**, p 18–25. https://doi.org/10.1016/j.jmapro.2019.01.048
34. F. Ren, J. Chen, and F. Chen, Constitutive Modeling of Hot Deformation Behavior of X20Cr13 Martensitic Stainless Steel with Strain Effect, *Trans. Nonferrous Met. Soc. China.*, 2014, **24**, p 1407–1413. https://doi.org/10.1016/S1003-6326(14)63206-4
35. W. Li, H. Li, Z. Wang, and Z. Zheng, Constitutive Equations for High Temperature Flow Stress Prediction of Al-14Cu-7Ce Alloy, *Mater. Sci. Eng. A.*, 2011, **528**, p 4098–4103. https://doi.org/10.1016/j.msea.2011.01.076
36. L. Chen, G. Zhao, J. Yu, W. Zhang, and T. Wu, Analysis and Porthole Die Design for a Multi-Hole Extrusion Process of a Hollow, Thin-Walled Aluminum Profile, *Int. J. Adv. Manuf. Technol.*, 2014, **74**, p 383–392. https://doi.org/10.1007/s00170-014-6003-4
37. C. Zhang, G. Zhao, H. Chen, Y. Guan, and F. Kou, Numerical Simulation and Metal Flow Analysis of Hot Extrusion Process for a Complex Hollow Aluminum Profile, *Int. J. Adv. Manuf. Technol.*, 2012, **60**, p 101–110. https://doi.org/10.1007/s00170-011-3609-7
38. A. Farjad Bastani, T. Aukrust, and S. Brandal, Optimisation of Flow Balance and Isothermal Extrusion of Aluminium Using Finite-Element Simulations, J. Mater. Process. Technol. 211 (2011) 650–667. https://doi.org/10.1016/j.jmatprotec.2010.11.021
39. F. Parvizian, T. Kayser, C. Hortig, and B. Svendsen, Thermomechanical Modeling and Simulation of Aluminum Alloy Behavior During Extrusion and Cooling, *J. Mater. Process. Technol.*, 2009, **209**, p 876–883. https://doi.org/10.1016/j.jmatprotec.2008.02.076
40. S.K. Jha, N. Keskar, K.I. Vishnu Narayan, K.V. Mani Krishna, D. Srivastava, G.K. Dey, and N. Saibaba, Microstructural and Textural Evolution During Hot Deformation of Dilute Zr-Sn alloy, J. Nucl. Mater. 482 (2016) 12–18. https://doi.org/10.1016/j.jnucmat.2016.09.028
41. L. Saintoyant, L. Legras, and Y. Bréchet, Effect of an Applied Stress on the Recrystallization Mechanisms of a Zirconium Alloy, *Scr. Mater.*, 2011, **64**, p 418–421. https://doi.org/10.1016/j.scriptamat.2010.11.003
42. M.E. Kassner, M.T. Perez Prado, T.A. Hayes, L. Jiang, S.R. Barrabes, and I.F. Lee, Elevated Temperature Deformation of Zr to Large Strains, J. Mater. Sci. 48 (2013) 4492–4500. https://doi.org/10.1007/s10853-012-7060-4
43. C. Zener and J.H. Hollomon, Effect of Strain Rate Upon Plastic Flow of Steel, *J. Appl. Phys.*, 1944, **15**, p 22–32
44. S.S. Zhou, K.K. Deng, J.C. Li, K.B. Nie, F.J. Xu, H.F. Zhou, and J.F. Fan, Hot Deformation Behavior and Workability Characteristics of Bimodal Size SiCp/AZ91 Magnesium Matrix Composite with Processing Map, *Mater. Des.*, 2014, **64**, p 177–184. https://doi.org/10.1016/j.matdes.2014.07.039
45. Y. Sun, Z. Wan, L. Hu, and J. Ren, Characterization of Hot Processing Parameters of Powder Metallurgy TiAl-Based Alloy Based on the Activation Energy Map and Processing Map, *Mater. Des.*, 2015, **86**, p 922–932. https://doi.org/10.1016/j.matdes.2015.07.140
46. J. Li, F. Li, and J. Cai, Constitutive Model Prediction and Flow Behavior Considering Strain Response in the Thermal Processing for the TA15 Titanium Alloy, *Materials.*, 2018, **11**, p 1985. https://doi.org/10.3390/ma11101985
47. A. Cingara and H.J. McQueen, New Formula for Calculating Flow Curves from High Temperature Constitutive Data for 300 Austenitic Steels, *J. Mater. Process. Technol.*, 1992, **36**, p 31–42. https://doi.org/10.1016/0924-0136(92)90236-L
48. D. Samantaray, S. Mandal, and A.K. Bhaduri, Constitutive Analysis to Predict High-Temperature Flow Stress in Modified 9Cr-1Mo (P91)

Steel, *Mater. Des.*, 2010, **31**, p 981–984. https://doi.org/10.1016/j.matdes.2009.08.012

49. H.L. Gegel, J.C. Malas, S.M. Doraievelu, and V.A. Shende, Metals Handbook, Vol. 14 (American Society for Metals, Metals Park, Ohio 1987), n.d
50. J.L.F. Aymone, E. Bittencourt, and G.J. Creus, Simulation of 3D Metal-Forming Using an Arbitrary Lagrangian-Eulerian Finite Element Method, *J. Mater. Process. Technol.*, 2001, **110**, p 218–232. https://doi.org/10.1016/S0924-0136(00)00886-4
51. C. Zhang, G. Zhao, Z. Chen, H. Chen, and F. Kou, Effect of Extrusion Stem Speed on Extrusion Process for a Hollow Aluminum Profile, *Mater. Sci. Eng. B.*, 2012, **177**, p 1691–1697. https://doi.org/10.1016/j.mseb.2011.09.041